

Influence of Electrification on Microphysical and Dynamical Processes in a Numerically Simulated Thunderstorm

ANPING SUN AND HYE-YEONG CHUN

Department of Atmospheric Sciences, Yonsei University, Seoul, Korea

JONG-JIN BAIK*

Department of Environmental Science and Engineering, Kwangju Institute of Science and Technology, Kwangju, Korea

MUHONG YAN

Cold and Arid Regions Environmental and Engineering Research Institute, Chinese Academy of Sciences, Lanzhou, China

(Manuscript received 30 July 2001, in final form 17 May 2002)

ABSTRACT

A new three-dimensional dynamics and electrification coupled model is developed to investigate the influence of electrification on microphysical and dynamical processes in thunderstorms. This model includes a four-class ice microphysics scheme, five electrification mechanisms, and lightning parameterization. Comparisons between model results and observations reveal that the dynamics and electrification coupled model is capable of reproducing many of the observed characteristics of the thunderstorm in dynamical, microphysical, and electrical aspects. The effects of electrification on microphysical and dynamical processes are examined by performing two numerical experiments, one with electrification processes and the other without them. Results show that when electrification processes are included the mass transfer among hydrometeors in microphysical processes, especially collection and coalescence processes, changes considerably as a result of significant modification of the terminal velocities of large precipitation particles. The change of mass transfer in microphysical processes affects cloud buoyancy by changing the amount and distribution of hydrometeors, and latent-heat release in the middle region of the thunderstorm increases. That is, convection strengthens by including electrification processes. The amount of solid precipitation and the diameter of solid precipitation particles at the surface increase because a stronger updraft sustains large precipitation particles and prevents them from falling out of the cloud earlier.

1. Introduction

During the past several decades, much effort has been made in numerical modeling of electrification processes in thunderstorms. Chiu (1978) developed a two-dimensional dynamics and electrification coupled model in which only warm microphysical processes were included. Takahashi (1984) incorporated ice microphysical processes with a riming electrification mechanism and examined electrification processes in a summertime thunderstorm. His results show that the polarity of charge transfer in the collision process depends on temperature and liquid water content. Below a critical tem-

perature in the range of -10° to -20°C , negative charge is transferred to graupel; in higher temperatures, positive charge is transferred. Updrafts carry small ice particles upward, forming positive charge in the upper region of the thunderstorm.

Helsdon and Farley (1987) investigated electrification processes in a thunderstorm that occurred in Montana on 19 July 1981 and showed that the noninductive electrification mechanism is a very important process. Ziegler and MacGorman (1994) examined the effectiveness of a noninductive charging mechanism in thunderstorms. They showed that the noninductive charging mechanism is one of the important electrification processes depending on liquid water content. Schuur and Rutledge (2000) simulated the evolution of electrical structure in the stratiform region of the mesoscale convective system (MCS) that occurred during the period of the Oklahoma–Kansas Preliminary Regional Experiment for Stormscale Operational and Research Meteorology (PRE-STORM). Their simulation results indicate that as much as 70% of the total charge in the

* Current affiliation: School of Earth and Environmental Sciences, Seoul National University, Seoul, Korea.

Corresponding author address: Prof. Hye-Yeong Chun, Department of Atmospheric Sciences, Yonsei University, 134 Shinchondong, Seodaemun-ku, Seoul 120-749, Korea.
E-mail: chy@atmos.yonsei.ac.kr

stratiform region is contributed by the noninductive ice–ice charging mechanism. There have been some laboratory studies on ice–ice charge separation (e.g., Jayaratne et al. 1983; Baker et al. 1987), which point out the importance of ice–ice collision for charge generation and separation in thunderstorms.

Even though electrification processes were included together with the dynamical and microphysical parts in the numerical models mentioned above, the effects of electrification on microphysical and dynamical processes in thunderstorms were not particularly considered. Variations in the terminal velocities of hydrometeors can result in the change of mass transfer in microphysical processes. As a consequence, the amount and distribution of all kinds of hydrometeors may be altered, which can, in turn, influence cloud buoyancy in a thunderstorm.

In an effort to realize the effects of thunderstorm electrification on microphysical and dynamical processes, a three-dimensional dynamics and electrification coupled model is developed, and numerical experiments are performed with the initial soundings taken from the Cooperative Convective Precipitation Experiment (CCOPE). To demonstrate the model's capability, comparisons between simulation results and observations are first made. Then, results concerning differences in microphysical and dynamical processes between experiments with and without electrification processes are presented and discussed.

2. Model description

The dynamical framework of the present model is similar to that established by Klemp and Wilhelmson (1978) except that three components of electric force per unit mass of moist air, $(\rho_T/\rho)E_x$, $(\rho_T/\rho)E_y$, and $(\rho_T/\rho)E_z$, are included in the momentum equations [see (1), (2), and (3), respectively]. That is, this model is a dynamics and electrification coupled model, which can be used to examine the spatial and temporal characteristics of space charge in thunderstorms and the effects of electrification on microphysical and dynamical processes. The governing equations for momentum in the horizontal and vertical directions, thermodynamic energy, and mass continuity can be written as

$$\frac{du}{dt} + c_p \bar{\theta}_v \frac{\partial \pi}{\partial x} = \frac{\rho_T}{\rho} E_x + D_u, \quad (1)$$

$$\frac{dv}{dt} + c_p \bar{\theta}_v \frac{\partial \pi}{\partial y} = \frac{\rho_T}{\rho} E_y + D_v, \quad (2)$$

$$\frac{dw}{dt} + c_p \bar{\theta}_v \frac{\partial \pi}{\partial z} = g \left(\frac{\theta'}{\bar{\theta}} + 0.608q'_v - q_T \right) + \frac{\rho_T}{\rho} E_z + D_w, \quad (3)$$

$$\frac{d\theta}{dt} = Q_{vl} + Q_{li} + Q_{vi} + D_\theta, \quad \text{and} \quad (4)$$

$$\begin{aligned} \frac{d\pi}{dt} + \frac{\bar{c}^2}{c_p \bar{\rho} \bar{\theta}_v^2} \frac{\partial}{\partial x_j} (\bar{\rho} \bar{\theta}_v u_j) \\ = \frac{R_d}{c_v} \pi \frac{\partial u_j}{\partial x_j} + \frac{c^2}{c_p \bar{\theta}_v^2} \frac{d\theta_v}{dt} + D_\pi, \end{aligned} \quad (5)$$

where $d/dt = \partial/\partial t + u_j \partial/\partial x_j$. Here, u , v , and w are the velocity components in the x , y , and z directions, respectively; θ is the potential temperature; θ' is the perturbation potential temperature; $\bar{\theta}_v$ is the virtual potential temperature; q_T is the mixing ratio of total hydrometeors; q'_v is the perturbation water vapor mixing ratio; π is the nondimensional perturbation pressure from the initial state; and ρ is the air density. Variables with an overbar denote those in the initial state that are functions of z only; R_d is the gas constant for dry air; c_p is the specific heat of air at constant pressure; c_v is the specific heat of air at constant volume; c is the adiabatic sound speed; and g is the gravitational acceleration. In (4), Q_{ab} represents the heating or cooling as a result of water phase change from status a to b or vice versa. The subscripts v , l , and i indicate water vapor, liquid water, and ice, respectively. These terms are described in appendix A. Furthermore, ρ_T is the total space charge density, and E_x , E_y , and E_z are the components of the electric field in the x , y , and z directions, respectively. The term D represents the turbulent diffusion and is evaluated with a prognostic equation for turbulent kinetic energy k . The term $d\theta_v/dt$ in (5) can be represented by

$$\frac{1}{\theta_v} \frac{d\theta_v}{dt} = \frac{1}{\theta} (Q_{vl} + Q_{li} + Q_{vi}) + 0.608S_{q_v}, \quad (6)$$

where S_{q_v} denotes the source and sink terms for water vapor.

The prognostic equations for the hydrometeor mixing ratio q_x and the number of hydrometeors per unit mass of air N_y can be written as

$$\frac{dq_x}{dt} = S_{q_x} + D_{q_x} + \frac{1}{\bar{\rho}} \frac{\partial}{\partial z} (\bar{\rho} q_x V_x) \quad \text{and} \quad (7)$$

$$\frac{dN_y}{dt} = S_{N_y} + D_{N_y} + \frac{1}{\bar{\rho}} \frac{\partial}{\partial z} (\bar{\rho} N_y V_y), \quad (8)$$

respectively. The mass-weighted average fall speeds are represented by V_x and V_y . Here, q_x includes water vapor and six hydrometeors (cloud water, rain, cloud ice, snow, graupel, and hail). The fall speeds of cloud water and cloud ice are considered when electrification processes are included, and they are assumed to be zero without electrification processes. Included in N_y are rain, cloud ice, snow, graupel, and hail (the number of cloud water drops per unit mass of air is specified). Notice that ρN_y is the number density of hydrometeor (m^{-3}). Parameterizations of microphysics in this model are based on the work of Orville and Kopp (1977) and Tripoli and Cotton (1982). Described in appendix A are S_{q_x} and S_{N_y} , which represent the source and sink terms

of mixing ratio and number (in unit mass of air) of each hydrometeor, respectively.

Each of the six hydrometeors is allowed to have charges associated with it. In the present model, five charging mechanisms, that is, inductive, noninductive, ion diffusion, selective ion capture, and secondary ice electrification, are simultaneously taken into account. Raindrop–cloud water drop inductive charging parameterization is based on the work of Chiu (1978). Parameterizations of inductive charging for ice particles and noninductive charging follow the work of Kuettner et al. (1981). Parameterizations of ion diffusion and selective ion capture are based on the work of Chiu (1978). For charge separation associated with secondary ice crystal production, the idea of Hallett and Saunders (1979) is adopted. More details about inductive and noninductive charging parameterizations are given in appendix B. The governing equation for the charge mixing ratio of each hydrometeor ($C \text{ kg}^{-1}$) is given by

$$\frac{dq_{xe}}{dt} = S_{d_{xe}} + D_{d_{xe}} + \frac{1}{\bar{\rho}} \frac{\partial}{\partial z} (\bar{\rho} q_{xe} V_x), \quad (9)$$

where q_{xe} denotes the charge mixing ratio carried by each hydrometeor, and $S_{d_{xe}}$ is the source and sink terms of the charge mixing ratio. Notice that ρq_{xe} is the charge density ($C \text{ m}^{-3}$). Detailed expressions of $S_{d_{xe}}$ are given in appendix B. In addition, the present model accounts for the presence of ions. The equation governing the number of positive (negative) ions per unit mass of air is given by

$$\begin{aligned} \frac{dn_{\pm}}{dt} = S_{n_{\pm}} + D_{n_{\pm}} \mp \frac{\partial}{\partial x} (\mu_{\pm} E_x n_{\pm}) \\ \mp \frac{\partial}{\partial y} (\mu_{\pm} E_y n_{\pm}) \mp \frac{\partial}{\partial z} (\mu_{\pm} E_z n_{\pm}), \end{aligned} \quad (10)$$

where μ_{\pm} is the ion mobility depending on height and is expressed by (Chiu 1978)

$$\mu_{+} = 1.4 \times 10^{-4} \exp(1.4 \times 10^{-4} z) \quad \text{and} \quad (11)$$

$$\mu_{-} = 1.9 \times 10^{-4} \exp(1.4 \times 10^{-4} z). \quad (12)$$

The source and sink terms of ions are $S_{n_{\pm}}$ (appendix B). The electric field can be obtained by the following equations:

$$\begin{aligned} E_x = -\frac{\partial \varphi}{\partial x}, \quad E_y = -\frac{\partial \varphi}{\partial y}, \\ E_z = -\frac{\partial \varphi}{\partial z}, \end{aligned} \quad (13)$$

$$\frac{\partial^2 \varphi}{\partial x^2} + \frac{\partial^2 \varphi}{\partial y^2} + \frac{\partial^2 \varphi}{\partial z^2} = -\frac{\rho_T}{\varepsilon}, \quad \text{and} \quad (14)$$

$$\rho_T = e\rho(n_{+} - n_{-}) + \sum \rho q_{xe}, \quad (15)$$

where φ is the electric potential, ε is the scalar electric permittivity of air, and e is the electronic charge ($1.6 \times 10^{-19} \text{ C}$).

TABLE 1. Prognostic variables in the dynamics and electrification coupled model.

Notation	Meaning
u	Velocity component in x direction
v	Velocity component in y direction
w	Velocity component in z direction
θ	Potential temperature
π	Nondimensional perturbation pressure
k	Turbulent kinetic energy
q_v	Mixing ratio of water vapor
q_c	Mixing ratio of cloud water
q_r	Mixing ratio of rain
q_i	Mixing ratio of cloud ice
q_s	Mixing ratio of snow
q_g	Mixing ratio of graupel
q_h	Mixing ratio of hail
N_r	Number of raindrops per unit mass of air
N_i	Number of ice particles per unit mass of air
N_s	Number of snow particles per unit mass of air
N_g	Number of graupel particles per unit mass of air
N_h	Number of hail particles per unit mass of air
q_{ce}	Charge mixing ratio of cloud water
q_{re}	Charge mixing ratio of rain
q_{ie}	Charge mixing ratio of cloud ice
q_{se}	Charge mixing ratio of snow
q_{ge}	Charge mixing ratio of graupel
q_{he}	Charge mixing ratio of hail
n_{+}	Number of positive ions per unit mass of air
n_{-}	Number of negative ions per unit mass of air

It is well known that lightning rearranges and neutralizes charges within thunderstorms (MacGorman and Rust 1998). The present model includes lightning parameterization (appendix C). Table 1 lists prognostic variables in the dynamics and electrification coupled model developed for this study.

In the present model, the standard staggered-mesh system by Klemp and Wilhelmson (1978) is employed, in which all thermodynamic, moisture, and electrical variables are defined at a common point, and the velocity components are displaced by one-half of a grid interval. In solving the compressible equations of motion, a time-splitting method is used. For the horizontal and vertical advection terms, fourth-order and second-order finite differences are used, respectively. The size of model domain is $35 \text{ km} \times 35 \text{ km} \times 18 \text{ km}$, with a horizontal grid interval of 500 m and a vertical grid interval of 250 m. The large and small time steps are 5 and 1 s, respectively. At the lateral boundaries, the radiation boundary condition is used for normal velocity. In addition, the normal mixing term and the first derivative of the horizontal electric field are assumed to be zero. At the model top, the vertical velocity and the mixing ratio, number per unit mass of air, and charge mixing ratio of hydrometeor are set to be zero, and the horizontal velocity, vertical component of the electric field, and ion number concentration are set equal to environmental values at the same height. Initially, the vertical profiles of the vertical component of the electric field and the number density of ions are specified as their environmental ones:

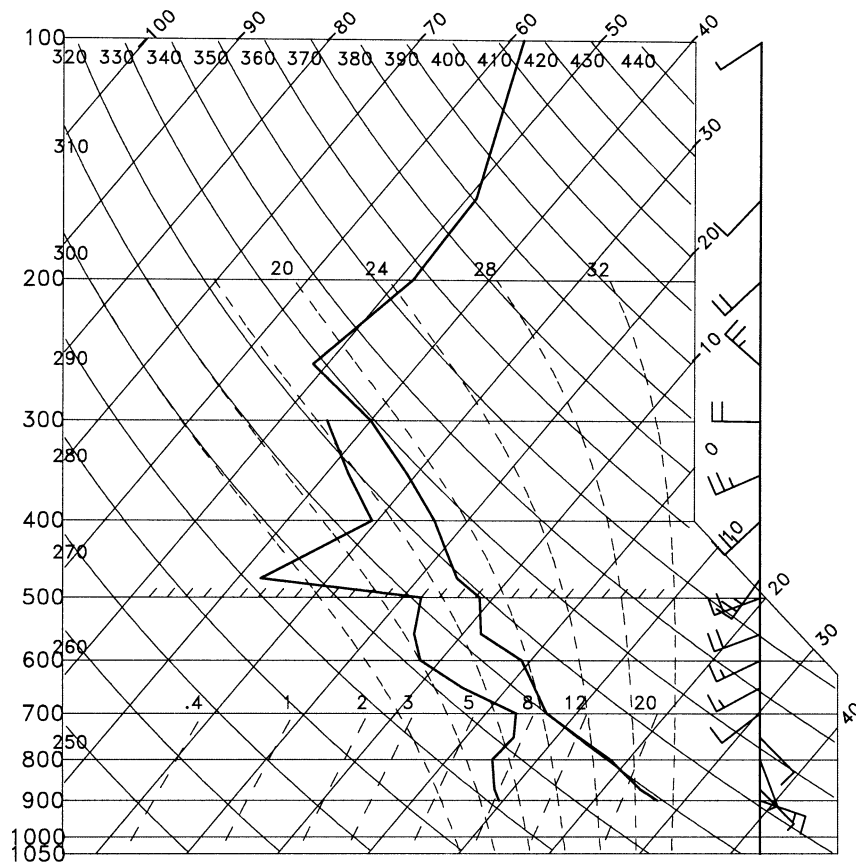


FIG. 1. Initial-state temperature and dewpoint temperature soundings on a skew T -log p diagram, together with initial-state horizontal velocity sounding.

$$E^0 = E_z^{00} \exp(-2 \times 10^{-4} z) \quad \text{and} \quad (16)$$

$$\rho n_{\pm}^0 = \frac{-1.7 \times 10^7}{E_z^{00}(\mu_+ + \mu_-)} \mp \frac{10^4 E_z^{00} \mu_{\pm}}{9.6 \pi(\mu_+ + \mu_-)}. \quad (17)$$

Here, $\pi = 3.14159$, and $E_z^{00} = -150 \text{ V m}^{-1}$ is used in the present study [$E_z^{00} = -100 \text{ V m}^{-1}$ was used in Chiu (1978)]. The initial profile of the number density of ions is based on the idea of Chiu (1978), which states that the number density of ions is due to the cosmic ray ionization at various heights and that the ionic recombination between ions of opposite polarities results in the annihilation of ions. The transport of ions in this fair-weather condition is assumed to be mainly controlled by electrical conduction. At the surface, the vertical velocity and electric potential are set equal to zero.

The initial-state wind, temperature, and moisture profiles used for numerical simulations are taken from observations in Montana on 19 July 1981 during the CCOPE period (Fig. 1). Using this sounding is beneficial because the detailed observational analyses of this case were presented in several studies (e.g., Jones et al. 1982; Gardiner et al. 1985; Dye et al. 1986), and, thus, simulated results can be directly compared with observations. Convection is initiated using a warm bubble with a maximum magnitude of 1.5 K located at the lowest

2 km of the model. Numerical integration is carried out for 90 min. There was one lightning flash observed in this storm at 1637 LST (Dye et al. 1986).

3. Results and discussion

The main purpose of this study is to investigate the effects of electrification on microphysical and dynamical processes in thunderstorms. For this, two numerical simulations, one with electrification processes (EC) and the other without them (NEC), are performed. To assess the model's capability of simulating natural thunderstorms, simulated results are first compared with observations.

a. Comparisons with observations

There are several studies that analyzed the thunderstorm that occurred on 19 July 1981 during the CCOPE period. Jones et al. (1982) reported National Center for Atmospheric Research sailplane-ascent results, and Gardiner et al. (1985) presented Aero Commander airplane data analysis results. Detailed observing platforms and observations were reported by Dye et al. (1986, hereinafter D86). In the case of a locally developed thun-

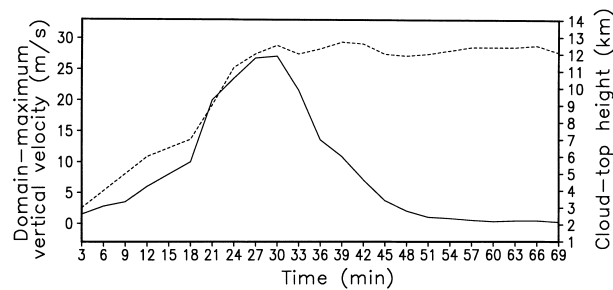


FIG. 2. Time series of domain-maximum vertical velocity (solid line) and cloud-top height (dashed line) in the EC simulation.

derstorm that exhibits a well-defined life cycle, a timing correspondence between simulated and observed thunderstorms is better to be set on the basis of the beginning of the rapid growth phase (Helsdon and Farley 1987). In the observed thunderstorm, this rapid growth phase began at about 1617 LST when the cloud-top height was near 7 km. At 1637 LST, a lightning flash was observed (D86). In the model thunderstorm (EC simulation), rapid growing begins at $t = 18$ min when the cloud top reaches 6.8 km (Fig. 2). That is, $t = 18$ min in the numerical simulation is considered to correspond to 1617 LST in the observation. At $t = 37$ min, there was a simulated lightning event.

In the model, the lightning parameterization is activated when the electric field exceeds a breakdown value (set to be 250 kV m^{-1} in this study). The processes of charge rearrangement and neutralization are taken into account to keep the electric field beneath the breakdown value. At $t = 37$ min, the maximum value of the vertical electric field is 288 kV m^{-1} , but it is reduced to 54 kV m^{-1} immediately after the activation of the lightning parameterization. Therefore, the electric field produced by this model would not be above the breakdown value in the whole domain during the simulation.

Norville et al. (1991) also simulated the 19 July 1981 thunderstorm. Their numerical model is 1.5-dimensional and includes explicit cloud microphysical parameterization and noninductive charging processes, but the dynamics are decoupled from the microphysics. Notice that our model is a three-dimensional, fully coupled model with bulk cloud microphysical parameterization, inductive and noninductive charging processes, and lightning parameterization. Their model produced a

maximum electric field of 127 kV m^{-1} , about one-half of the value of the maximum electric field in the present simulation (288 kV m^{-1}). The maximum electric field occurred very close to the time of the observed discharge. This is similar to our result.

The simulated thunderstorm experienced a single-cell life cycle, which developed in a moderately unstable environment with a weak vertical wind shear (Fig. 1). The convective available potential energy (CAPE) of the initial thermodynamic sounding is 427 J kg^{-1} . Table 2 presents a summary of comparisons between the simulated and observed features of the thunderstorm. The observed data are extracted from D86. The cloud-base height in the EC simulation maintains 3 km, which is a little bit lower than the observed one. This discrepancy is most likely due to the initial sounding used for the numerical simulation. Based on an examination of the aircraft data, Helsdon and Farley (1987) pointed out that the boundary layer is more variable in moisture and drier than that observed at the time of the sounding. A drier environment would lead to a higher cloud base. The updraft begins to intensify rapidly at $t = 18$ min (1617 LST for the observed thunderstorm), and the rapid growth period persists until $t = 30$ min, at which time the maximum vertical velocity starts to decrease (Fig. 2). During the rapid growth period, the cloud-top height increases from 6.8 to 12.5 km, and the most actively growing region shifts toward the downwind side of the thunderstorm. The model-produced maximum cloud-top height (12.5 km) is 2 km higher than the observed one (10.5 km). This amount of difference is within an observational error of cloud-top height (Jones et al. 1982). The rate of cloud-top rise during the rapid growth phase ($5\text{--}9 \text{ m s}^{-1}$) agrees well with the observation ($5\text{--}7 \text{ m s}^{-1}$). The domain-maximum vertical velocity during the thunderstorm lifetime is 27.1 m s^{-1} at $z = 8.2 \text{ km}$, which is much stronger than was observed. A possible reason for the relatively weak maximum vertical velocity in the observation is that the aircraft measurement was hardly made in the main updraft area of the thunderstorm.

Figure 3 shows the vertical cross-sectional fields of liquid water and graupel contents at $t = 30$ and $t = 27$ min, respectively, at the time that the observational data are available. These are at $y = 18 \text{ km}$. The maximum liquid water content predicted by the model is 3.8 g m^{-3}

TABLE 2. Quantitative comparisons between model results and observations.

Feature	Model (EC)	Observation
Rapid growth phase	18–30 min	1617–1630 LST
Cloud-base height	3.0 km	3.8 km
Max cloud-top height	12.5 km	10.5 km
Max vertical velocity	27.1 m s^{-1}	$10\text{--}15 \text{ m s}^{-1}$
Start of updraft decay	30 min	1632 LST
Cloud-top rise rate	$5\text{--}9 \text{ m s}^{-1}$	$5\text{--}7 \text{ m s}^{-1}$
Max liquid water content	3.8 g m^{-3} at 8.0 km	2.5 g m^{-3} at 7.0 km
Graupel/hail appearance	27 min at 5.0 km	1626 LST at 5.8 km

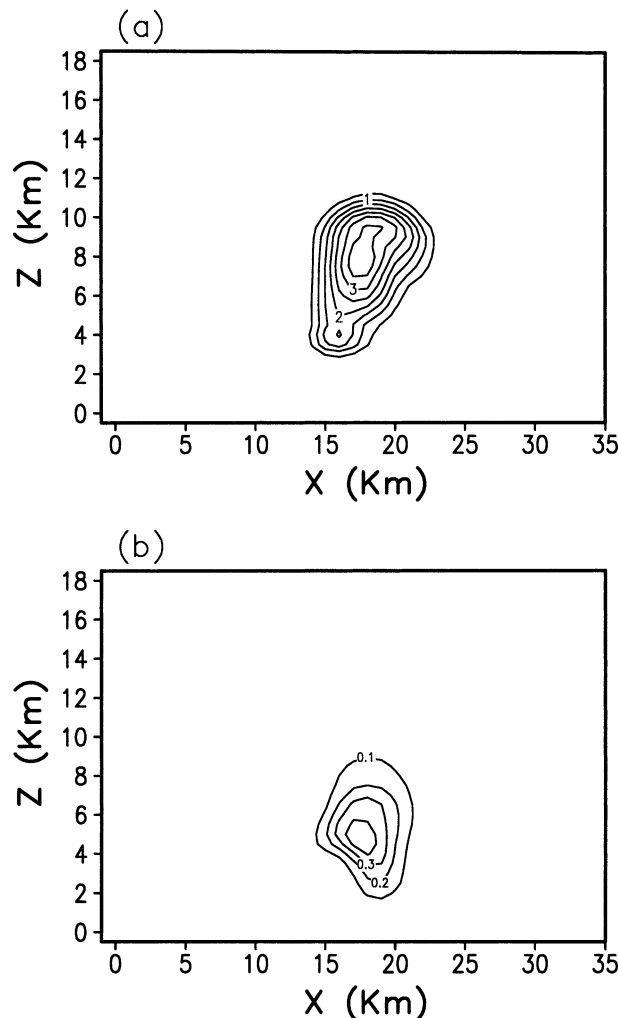


FIG. 3. Vertical cross section (x - z plane) of (a) liquid water content at $t = 30$ min and (b) graupel content at $t = 27$ min in the EC simulation at $y = 18$ km. The contour intervals of (a) and (b) are 0.5 and 0.1 g m^{-3} , respectively.

at $z = 8$ km (Fig. 3a), whereas that measured in the actual thunderstorm is 2.5 g m^{-3} at $z = 7$ km at 1630 LST. One of the possible reasons for this difference is that the initial relative humidity used for the numerical simulation is higher than that in the real boundary layer when the thunderstorm occurred. The time that graupel or hail particles appear agrees well with the observed time, but the appearance height is slightly lower than was observed (Fig. 3b and Table 2).

Figure 4 shows simulated total charge density fields at $t = 36$ and 40 min. These two times correspond to the first and second times of three aircraft penetrations at $z = 4.5$ km (Helsdon and Farley 1987). At $t = 36$ min, a region of positive charge density greater than 0.2 nC m^{-3} is located between $z = 8$ and 12 km (note that the cloud-top height at this time is 12.5 km), and a region of negative charge density greater than 0.2 nC m^{-3} is located between $z = 5$ and 8 km. The maximum

negative charge density near $z = 5$ km is about -0.2 nC m^{-3} , which is about one-half of what was observed (-0.4 nC m^{-3}) (Helsdon and Farley 1987). At $t = 40$ min, the negative charge density increases by about two times that at $t = 36$ min, and the maximum negative charge density region goes down to $z = 5$ km. This is qualitatively consistent with the fact that the negative charge region lowers as rimed precipitation particles appear in the thunderstorm.

The above comparisons indicate that many of the microphysical, dynamical, and electrical characteristics of the thunderstorm revealed by aircraft measurements are generally reproduced in the numerical simulation. Thus, it is possible to study dynamical, microphysical, and electrical processes of thunderstorms using the present model, and simulation results will be credible.

b. Influence of electrification on terminal velocity

Figure 5 shows the vertical cross-sectional fields of difference in the terminal velocity of graupel between the EC and NEC simulations (Fig. 5a), terminal velocity of graupel in the NEC simulation (Fig. 5b), charge density of graupel (Fig. 5c), and vertical component of electric field (Fig. 5d) at $t = 42$ min. When electrification processes are not included, the maximum terminal velocity of graupel is slightly larger than 10 m s^{-1} at $z = 6$ and 10.5 km (Fig. 5b). When electrification processes are included, the terminal velocity of graupel decreases in the middle region of the thunderstorm by a maximum magnitude of 1.9 m s^{-1} , and it increases near the top of the thunderstorm by a maximum magnitude of 2.6 m s^{-1} (Fig. 5a). This can be explained with the intensity and distribution of vertical electric force $q_{ge}E_z$. Graupel particles are negatively charged with a peak value of -1.3 nC m^{-3} in the region of the positive vertical electric field with a peak value of 55 kV m^{-1} above $z = 10$ km. Thus, graupel particles are attracted downward by negative vertical electric force, and the terminal velocity of graupel increases. Below $z = 10$ km, the terminal velocity of graupel decreases because graupel particles experience a positive electric force.

To exploit the evolution of the upper negative charge density pocket associated with graupel, the time series of total charge density of graupel and contribution of each charging mechanism to the graupel charge density, graupel content, and difference in the terminal velocity for graupel at $z = 11$ km are plotted (not shown). Graupel reaches its maximum charge density at $t = 42$ min, and at this time the graupel-ice noninductive charging mechanism is dominant over the other charging mechanisms. The time when graupel content at $z = 11$ km reaches its maximum is earlier ($t = 36$ min) than the time of the maximum graupel charge density ($t = 42$ min) and the maximum difference in the terminal velocity ($t = 42$ min). The difference in the terminal velocity evolves very well with the development of graupel charge density. Therefore, the difference in the ter-

terminal velocity of graupel is generally due to the charge magnitude associated with graupel.

Figure 6 is the same as Fig. 5 except for hail. The terminal velocity of hail reaches its maximum value of 13.4 m s^{-1} at $z = 3.5 \text{ km}$ when electrification processes are not included (Fig. 6b). Because hail particles experience a positive electric force in the thunderstorm ($q_{he}E_z > 0$; see Figs. 6c,d), the terminal velocity of hail decreases by as much as 3.4 m s^{-1} at $z = 1.75 \text{ km}$ by electrification processes (Fig. 6a). In comparison with graupel, there is very little difference in terminal velocity above $z = 8 \text{ km}$. This is because hail particles are located in a relatively lower region at $t = 42 \text{ min}$ because it forms at lower levels because of stronger riming and wet growth in the thunderstorm.

c. Influence of electrification on microphysics

Collection and coalescence are important microphysical processes in cloud development and are strongly dependent upon the terminal velocities of hydrometeor particles. Considering that the terminal velocity of each hydrometeor, particularly larger particles, changes significantly by electrification, there should be some differences in microphysical processes between the EC and NEC simulations.

Table 3 shows the accumulated mass of hydrometeor in each microphysical process over the entire model domain at $t = 42 \text{ min}$ in the EC and NEC simulations; NU, CN, ML, CL, SU, CD, DE, and EV represent the nucleation, autoconversion, melting, collection and coalescence, sublimation, condensation, deposition, and evaporation, respectively. Among the 16 microphysical processes listed in Table 3, the accumulated mass increases by the first 6 processes and decreases by the rest because of electrification processes. The total amount of graupel transferred from cloud water through collection and coalescence process (CL_{cg}) increases by electrification processes by as much as 21%. This is mainly because the increased terminal velocity of graupel near the thunderstorm top (Fig. 5a) provides a better chance to collect more cloud drops, which have relatively small terminal velocity even in a strong electric environment. The accumulated mass of cloud water by the condensation process (CD_{vc}) increases by 20%. The accumulated mass of hydrometeor by each of the four microphysical processes (NU_{vi} , CL_{ig} , CN_{ig} , and DE_{vi}) in the EC simulation increases by less than 2% of the mass of hydrometeor in the NEC simulation. The largest percentage change of hydrometeor in microphysical processes by electrification processes occurs in the mass of ice by collecting cloud water (CL_{ci}), which decreases by as much as 50%. This is because the terminal velocity of ice particles (not shown) is retarded by electric force near the thunderstorm top. However, the mass transfer by this process is very small when compared with that by other processes. The mass of rain by the melting of

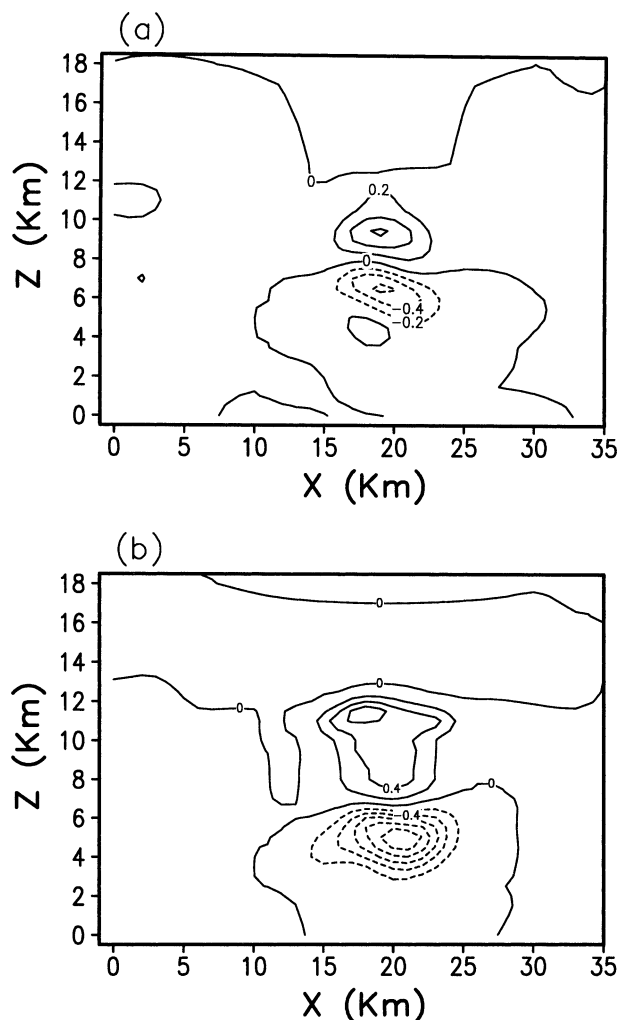


FIG. 4. Vertical cross section (x - z) of total charge density at (a) $t = 36$ and (b) $t = 40 \text{ min}$ in the EC simulation at $y = 18 \text{ km}$. Solid and dashed lines indicate positive and negative charge densities, respectively, and the contour interval is 0.2 nC m^{-3} .

graupel or hail decreases significantly because of electrification processes.

Next, the overall effects of electrification on microphysics are examined. For this, the total amounts of condensation and freezing, evaporation and melting, deposition, and sublimation over the entire model domain during the lifetime of the thunderstorm, the total amount of net moisture entering into the thunderstorm through the cloud base, and the latent heat released during microphysical processes are calculated. Results are listed in Table 4. The amount of condensation and freezing and the amount of deposition in the EC simulation increase by as much as 108% and 17%, respectively, by electrification processes. The enhancement of these two processes can be reasonably reflected in Table 3. There are five microphysical processes (CL_{ci} , CL_{cg} , CL_{rg} , CL_{ch} , and CL_{rh}) that contribute to the freezing process when cloud water or rain is collected by cloud ice, graupel

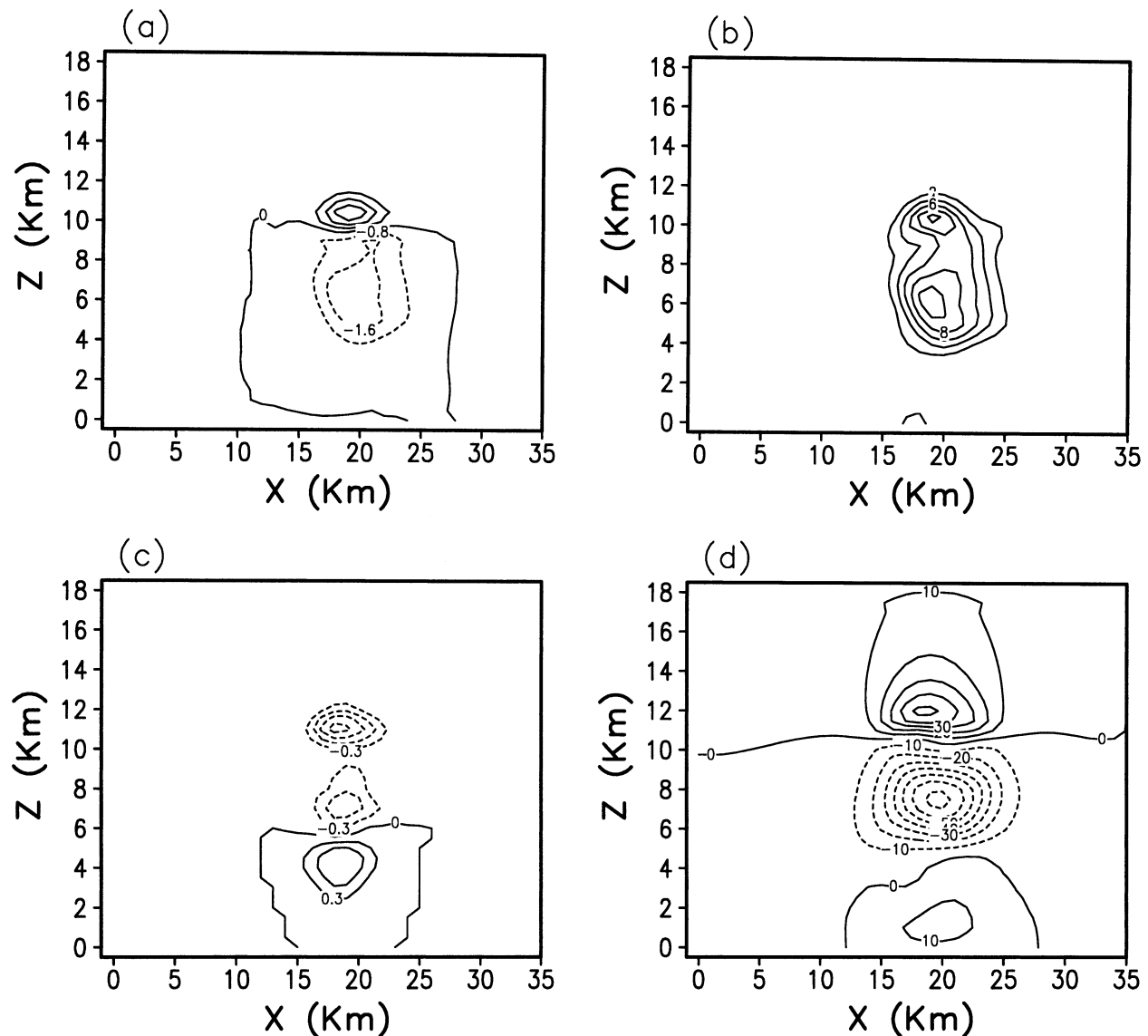


FIG. 5. Vertical cross section (x - z) of (a) difference in the terminal velocity of graupel between the EC and NEC simulations, (b) terminal velocity of graupel in the NEC simulation, (c) charge density of graupel in the EC simulation, and (d) vertical component of electric field in the EC simulation at $t = 42$ min and at $y = 18$ km. The contour intervals of (a), (b), (c), and (d) are 0.8 m s^{-1} , 2 m s^{-1} , 0.3 nC m^{-3} , and 10 kV m^{-1} , respectively.

pel, or hail particles and one microphysical process (CD_{ve}) that contributes to the condensation process. The mass of cloud water transferred from vapor increases by 576.9 kton ($1 \text{ kton} = 10^6 \text{ kg}$) (Table 3). Although the mass of cloud ice, graupel, and hail transferred from liquid to ice phase through the processes of CL_{ci} , CL_{rg} , CL_{ch} , and CL_{rh} decreases by 309.53 kton, the mass of graupel through the process of CL_{cg} increases by 409.35 kton by electrification processes. In contrast, the amount of evaporation and melting decreases by electrification processes. This is mainly because the mass increase of rain through the melting of hail (ML_{hr}) is significantly less in the EC simulation than in the NEC simulation. The amount by sublimation decreases slightly by elec-

trification processes because the mass increase of water vapor through the sublimation of hail (SU_{hv}) is small.

The microphysical processes examined above not only determine the amount and distribution of hydrometeors in the thunderstorm but also affect latent heat released in each microphysical process during the thunderstorm development. The total mass of conversion increases in condensation, freezing, and deposition processes and decreases in evaporation, melting, and sublimation processes when electrification processes are included. Latent heat released through microphysical processes increases from 8.67×10^{14} to $10.78 \times 10^{14} \text{ J}$. The increase of latent heat intensifies buoyancy in the thunderstorm. Therefore, the accumulated amount of net

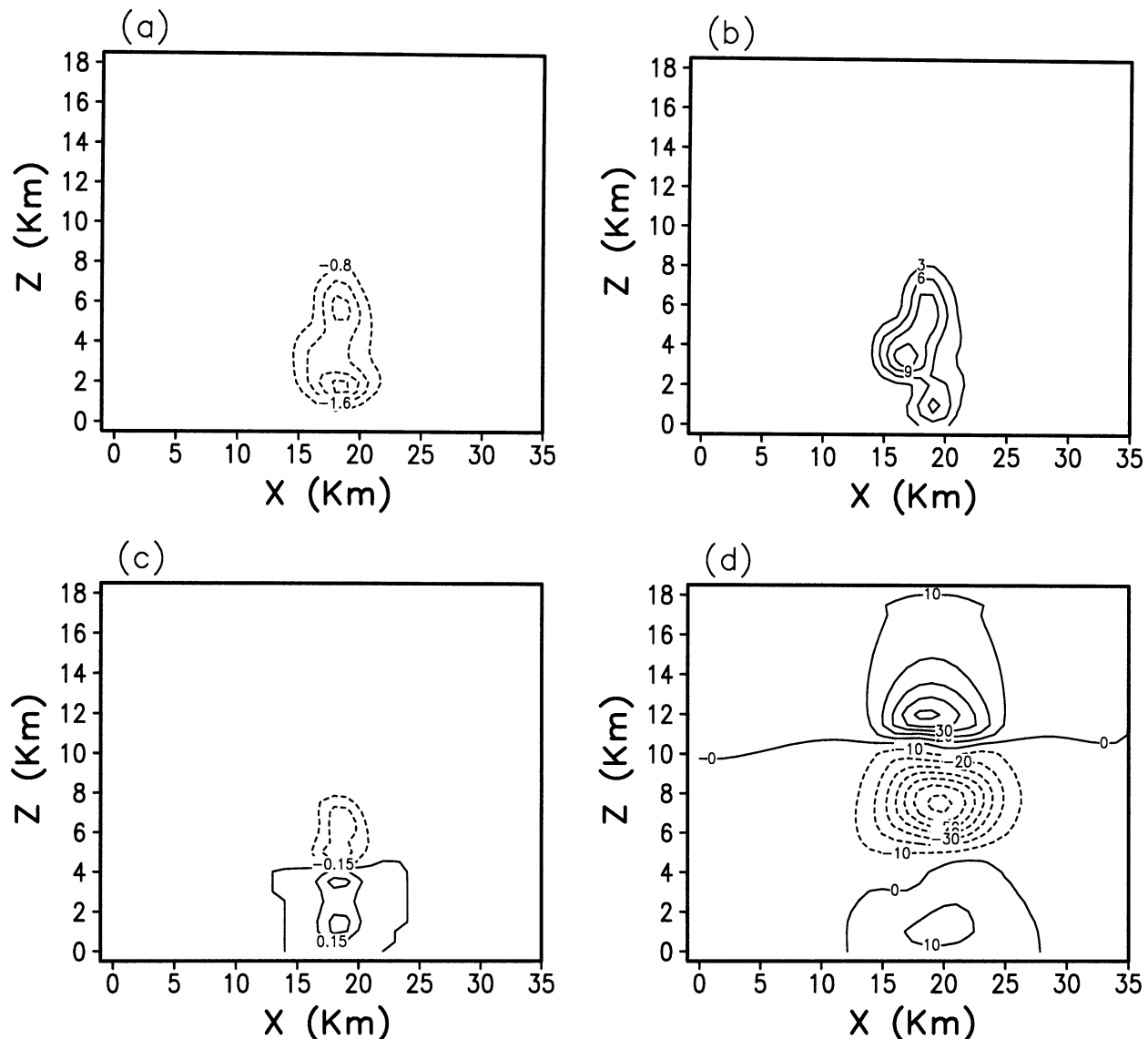


FIG. 6. The same as Fig. 5 but for hail. The contour intervals of (a), (b), (c), and (d) are 0.8 m s^{-1} , 3 m s^{-1} , 0.15 nC m^{-3} , and 10 kV m^{-1} , respectively.

moisture entering into the thunderstorm through the cloud base increases from 1.88×10^3 to 2.97×10^3 kton (as much as 58%).

Figure 7 shows the vertical cross-sectional field of perturbation potential temperature through the center of the thunderstorm in the y direction at $t = 42$ min. A main difference in the perturbation potential temperature field between the EC and NEC simulations is larger positive perturbation and its wider area above $z = 6$ km, centered at $x = 18$ km and $z = 8.5$ km in the EC simulation. As a result of enhanced collection and coalescence processes in the presence of a strong electric field and charged drops, larger and faster-falling precipitation particles form rapidly, which results in the

redistribution of hydrometeors with subsequent effects on cloud buoyancy and dynamics.

Figure 8 shows the time series of domain-maximum vertical electric force, buoyancy when the maximum vertical electric force occurs, and difference in domain-maximum vertical velocity between the EC and NEC simulations. Before $t = 24$ min, there are no differences in buoyancy and domain-maximum vertical velocity between the EC and NEC simulations because of weak electrification processes. Vertical electric force begins to intensify rapidly from $t = 24$ min, and the growth period persists until $t = 42$ min when the vertical electric force reaches its maximum value of 0.026 m s^{-2} (Fig. 8a). During the period with stronger vertical electric

TABLE 3. The accumulated mass (kton = 10^6 kg) of hydrometeor transferred in each microphysical process over the entire domain at $t = 42$ min in the EC and NEC simulations: NU, CN, ML, CL, CD, SU, DE, and EV denote the nucleation, autoconversion, melting, collection and coalescence, condensation, sublimation, deposition, and evaporation, respectively. The subscripts v , c , r , i , s , g , and h represent the water vapor, cloud water, rain, cloud ice, snow, graupel, and hail, respectively. For example, NU_{vi} denotes the accumulated mass of ice transferred by water vapor through the nucleation process.

Process	CL_{cg}	CD_{uc}	NU_{vi}	CL_{ig}	CN_{ig}	DE_{vi}
EC	2329.45	3452.1	11.48	332.98	58.23	2476.00
NEC	1920.10	2875.2	11.27	327.23	57.34	2438.12
Process	CL_{ci}	ML_{hr}	CL_{rh}	ML_{gr}	CL_{gh}	EV_{rv}
EC	1.36	2756.36	454.56	1826.34	635.56	768.90
NEC	2.70	3613.69	540.98	2056.91	707.36	830.89
Process	SU_{hv}	CL_{rg}	CN_{gh}	DE_{vg}		
EC	245.89	6655.13	3211.10	709.41		
NEC	265.31	6805.10	3245.12	711.81		

force ($t = 27$ – 51 min), buoyancy in the EC simulation is obviously larger than that in the NEC simulation. The difference in buoyancy between the EC and NEC simulations is 0.023 m s^{-2} at $t = 42$ min. The maximum difference in maximum vertical velocity between the EC and NEC simulations is 3.1 m s^{-1} at $t = 42$ min.

d. Influence of electrification on dynamics

Figure 9 shows the vertical cross-sectional field of the vertical component of vorticity ζ at $t = 42$ min and at the center of the thunderstorm in the y direction (at $y = 18$ km). By electrification processes, the vertical component of vorticity increases significantly in the region of $z = 4$ – 10 km. This indicates that electrification processes change not only thermodynamics but also dynamics. This is because the velocity changes directly by electric force and indirectly by thermodynamic variables through changed microphysical processes. The enhanced mesolow in the thunderstorm implies stronger updrafts and a larger amount of latent heating.

The local change of the vertical component of vorticity is determined by the following equation when the Coriolis force is negligible (Houze 1993):

$$\frac{\partial \zeta}{\partial t} = -\mathbf{V} \cdot \nabla \zeta + \zeta \frac{\partial w}{\partial z} + \left[\left(\frac{\partial u}{\partial z} - \frac{\partial w}{\partial x} \right) \frac{\partial w}{\partial y} + \left(\frac{\partial w}{\partial y} - \frac{\partial v}{\partial z} \right) \frac{\partial w}{\partial x} \right]. \quad (18)$$

TABLE 4. The accumulated amounts of condensation and freezing, evaporation and melting, deposition, and sublimation over the entire model domain during the lifetime of the thunderstorm, the accumulated amount of net moisture entering into the thunderstorm through the cloud base, and the latent-heat release during the microphysical processes in the EC and NEC simulations. The units are kilotons, except for latent heat, which is represented in joules $\times 10^{14}$.

Process	Condensation and freezing	Evaporation and melting	Deposition	Sublimation	Net moisture	Latent heat
EC	2.56×10^6	5.90×10^6	8.87×10^2	2.60×10^2	2.97×10^3	10.78
NEC	1.23×10^6	8.99×10^6	7.61×10^2	2.89×10^2	1.88×10^3	8.67

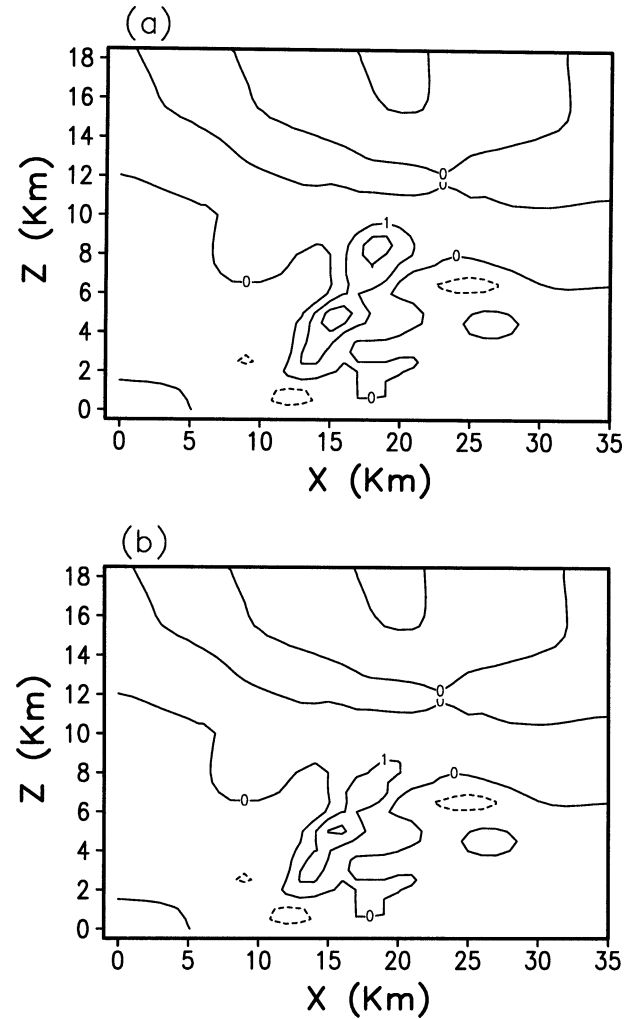


FIG. 7. Vertical cross section (x – z) of perturbation potential temperature at $t = 42$ min and at $y = 18$ km in the (a) EC and (b) NEC simulations. The contour interval is 1 K.

The three terms in the right-hand side of (18) represent the advection, stretching, and tilting terms, respectively. Figure 10 shows the difference in each term of (18) between the EC and NEC simulations at $z = 8$ km where the maximum ζ exists in the x – z cross section in Fig. 9. This figure shows that electrification processes enhance the local change of the vertical component of vorticity near the center and northern part of main updraft and reduce the local vorticity change near $y = 16$ –

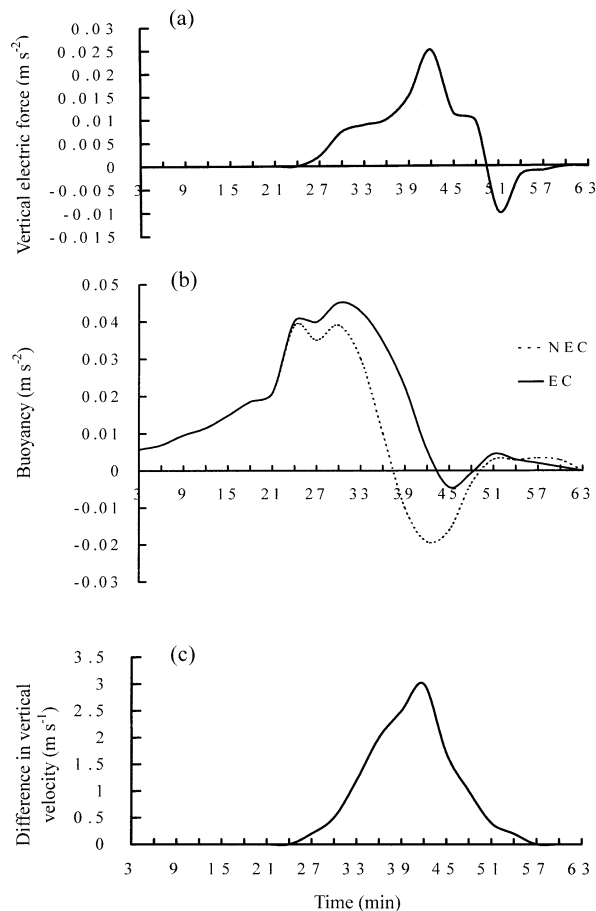


FIG. 8. Time series of (a) domain-maximum vertical electric force per unit mass of air $(\rho_T/\rho)E_z$, (b) buoyancy $g(\theta'/\bar{\theta} + 0.608q'_v - q_T)$ when the maximum vertical electric force occurs, and (c) difference in domain-maximum vertical velocity between the EC and NEC simulations.

20 km. These changes are due to the advection and stretching processes; the contribution by the tilting process is relatively small.

e. Influence of electrification on solid precipitation at the surface

Dynamical processes always interact with microphysical processes. Modified microphysics in an intensively electrified thundercloud alters the amount and distribution of water substance and affects cloud buoyancy by changing water loading. Enhanced convection, in turn, can influence cloud microphysics in a subtle way. As presented in Table 3, the total amounts of rain transferred from hail and graupel by the melting process are decreased by as much as 24% and 11%, respectively, by electrification processes. A stronger updraft in the thunderstorm sustains graupel and hail particles and prevents them from falling out of the cloud earlier. So, those precipitation particles have more time to be carried up by updraft and better opportunity to grow by col-

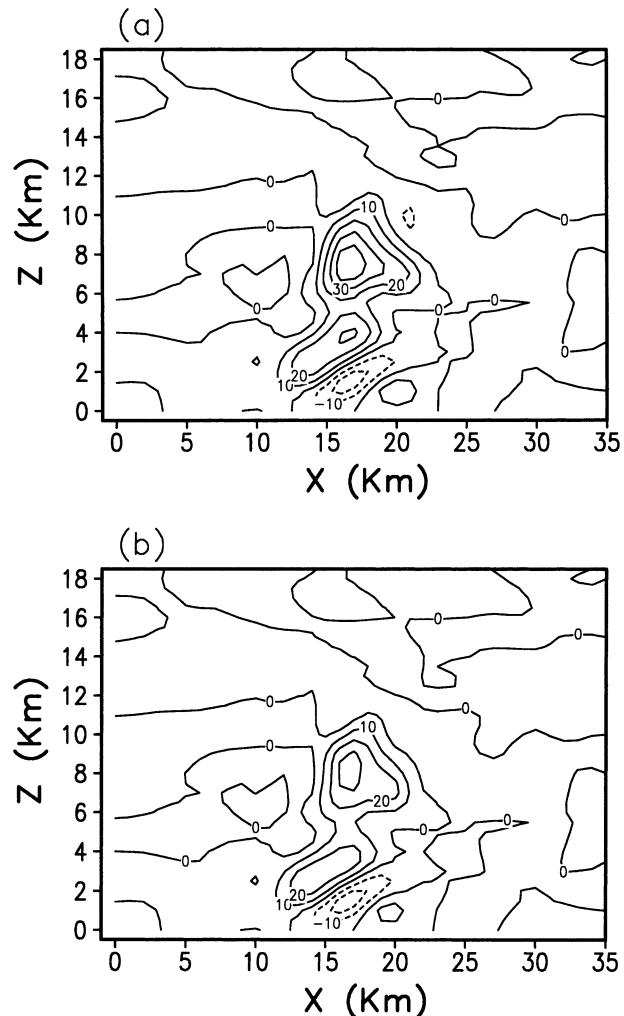


FIG. 9. Vertical cross section (x - z) of the vertical component of vorticity at $t = 42$ min and at $y = 18$ km in the (a) EC and (b) NEC simulations. The contour interval is $10 \times 10^{-4} \text{ s}^{-1}$.

lecting supercooled cloud drops and ice crystals. Therefore, the accumulated solid precipitation at the surface is larger, and the time that solid precipitation first reaches the surface is delayed by 3 min in the EC simulation as compared with the NEC simulation (Fig. 11a). The maximum diameter of solid precipitation particles at the surface is about 5.7 mm in the EC simulation, and it is about 5.0 mm in the NEC simulation (Fig. 11b). After $t = 46$ min, the maximum diameter of solid precipitation at the surface is consistently larger in the EC simulation because a stronger updraft and a decreased melting process from hail and graupel by electrification processes make precipitation particles larger.

4. Summary and conclusions

A three-dimensional dynamics and electrification coupled model was developed to investigate the effects of electrification on microphysical and dynamical pro-

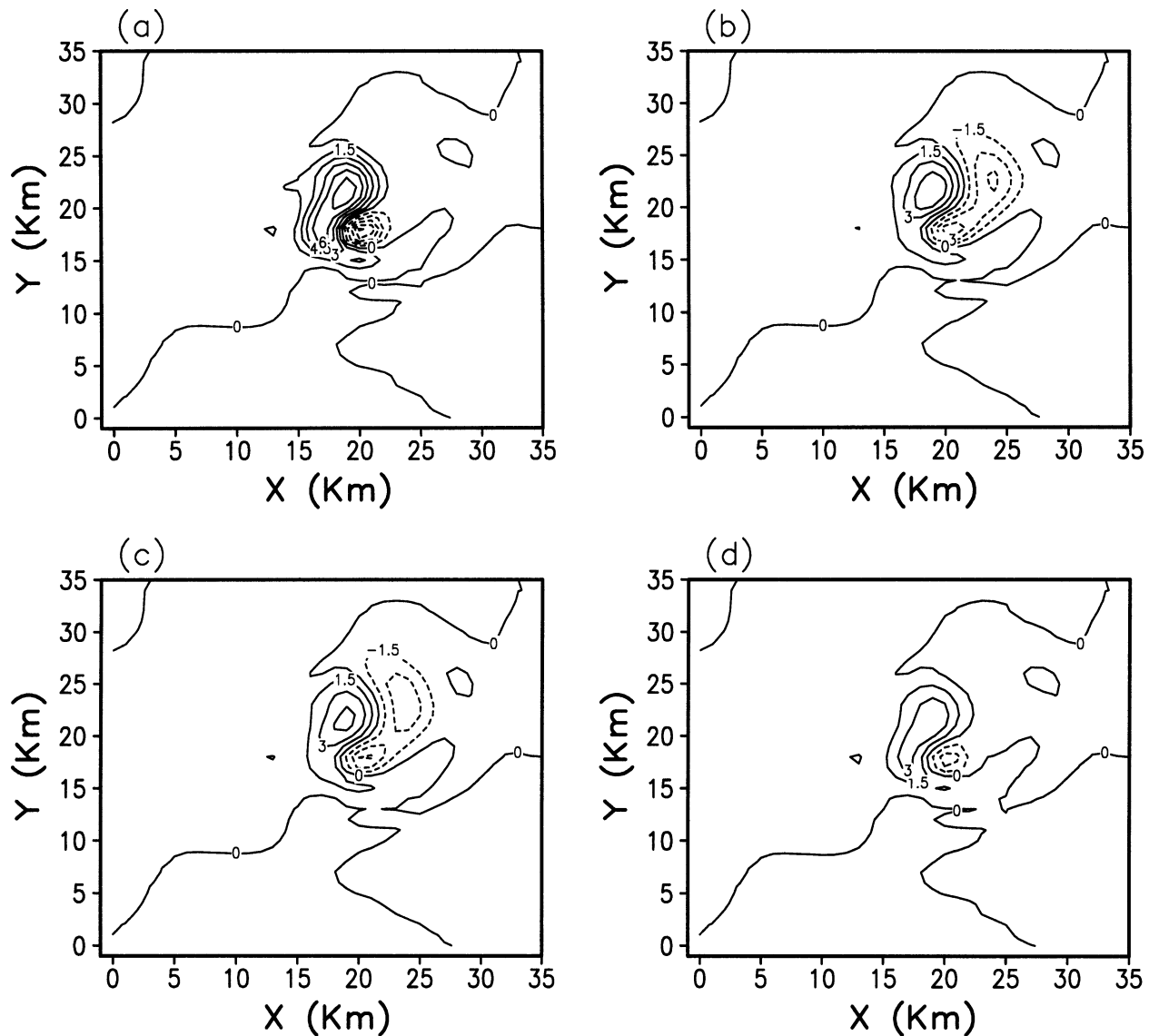


FIG. 10. Horizontal cross section (x - y) of difference in each term of the vorticity equation (18) between the EC and NEC simulations at $t = 42$ min and at $z = 8$ km; (a), (b), (c), and (d) differences in the local change of vorticity, vorticity advection, stretching, and tilting terms, respectively. The contour interval is $1.5 \times 10^{-5} \text{ s}^{-1}$.

cesses in thunderstorms. Numerical simulations were performed for the Montana thunderstorm that occurred on 19 July 1981. It was demonstrated that the coupled model can reproduce many of the observed characteristics of the thunderstorm reasonably well in microphysical, dynamical, and electrical aspects, which confirms that the present model is a good tool for investigating the overall structure and evolution of thunderstorms. The effects of electrification on microphysical and dynamical processes in thunderstorms were quantitatively discussed on the basis of two numerical experiments with and without electrification processes. Results indicated that the terminal velocities of hydrometeors, particularly larger particles, are affected by electrification processes. This was responsible for

changing masses and number concentrations of hydrometeors transferred during microphysical processes and the distribution of hydrometeors. Latent heat released in the middle part of the thunderstorm subsequently increased and updraft was intensified. The reinforced updraft can sustain growing precipitation particles and prevent them from falling out of the cloud earlier. Therefore, the amount of solid precipitation and the diameter of precipitation particles at the surface were larger when electrification processes were included.

In this study, the influence of electrification processes on microphysics and dynamics in thunderstorms was explained via the alteration of the terminal velocities of hydrometeors. Even though electrification processes can also change collision efficiencies between precipitation

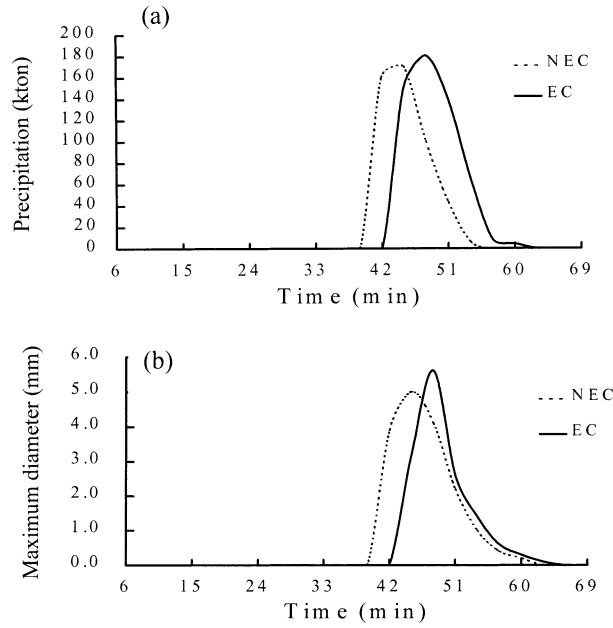


FIG. 11. Time series of (a) the total amount of solid precipitation and (b) the maximum diameter of solid precipitation particles at the surface in the EC (solid line) and NEC (dashed line) simulations.

particles, this effect was not taken into account in the present model. To simulate better the electrically active thunderstorms, collision efficiencies changed by electrification processes should be expressed based on theoretical works and laboratory experiments. This task remains for future research.

The noninductive charging parameterization used in the present model follows the work of Kuettner et al. (1981). The parameterization contains the basic necessities for modeling a charging process based on ice–ice collisions. However, many laboratory studies over the last 20 years have demonstrated that the magnitude and sign of charge separated per ice–ice collision are a strong function of temperature, (effective) liquid water content, and terminal fall speed of the larger ice particle (MacGorman and Rust 1998). Key details of the charging process and resulting electric field could be affected by these dependencies. An update of the noninductive charging parameterization based on laboratory studies is required.

The present electrification and dynamics coupled model uses a bulk cloud microphysical scheme. In a bulk model, detailed information on cloud microphysical processes in a size spectrum is not available. That is, only the overall effects of electrification on cloud microphysics and dynamics can be examined with a bulk model. In this sense, the effects of electrification on cloud microphysics and dynamics revealed in the present study might be exaggerated to some extent. This possibility can be deduced from observations indicating that only a small fraction of particles typically carry significant electrical charge (e.g., Gardiner et al. 1985)

and that charges of both signs are found at all levels within a thunderstorm even though the net charge typically follows the classic dipole pattern (e.g., Bateman et al. 1999). In the present study, the horizontal distribution of graupel charge density at various levels (not shown) reveals that negative and positive charges coexist at certain levels. Although there is a fundamental limitation of a bulk model in representing cloud microphysics, the electrification and dynamics coupled model using the bulk cloud microphysical scheme can be a reliable and efficient tool for investigating the overall structure and evolution of thunderstorms in three dimensions.

Acknowledgments. The authors are very grateful to three anonymous reviewers for providing constructive comments that led to improvements of the original manuscript. This research was supported by the Korea Ministry of Science and Technology through the National Research Laboratory Program, and the Brain Korea 21 Program.

APPENDIX A

Microphysical Terms

The diabatic terms from the phase change of water substance in (4) are

$$Q_{vi} = \frac{L_v}{c_p \bar{\Pi}} (CD_{vc} - EV_{cv} - EV_{rv}), \quad (A1)$$

$$Q_{li} = \frac{L_f}{c_p \bar{\Pi}} (P_{ci} + CL_{cg} + CL_{ch} + CL_{cs} + CL_{rg} + CL_{rh} - ML_{gr} - ML_{hr} - ML_{sr}), \quad \text{and} \quad (A2)$$

$$Q_{vi} = \frac{L_s}{c_p \bar{\Pi}} (NU_{vi} + SU_{vs} + SU_{vg} + SU_{vh} - DE_{hv} - DE_{gv} - DE_{sv}), \quad (A3)$$

where L_v , L_f , and L_s are the latent heat of evaporation, freezing, and sublimation, respectively; $\bar{\Pi} = (\bar{p}/p_0)^{R_d/c_p}$, where \bar{p} is the initial-state pressure and p_0 is the reference-level pressure. Other variables have the same meanings as in Table 3, except that P_{ci} is the ice enhancement process.

The source and sink terms of hydrometeor in (7) are

$$S_{qv} = EV_{cv} + EV_{rv} + SU_{iv} + SU_{sv} + SU_{gv} + SU_{hv} - (CD_{vc} + DE_{vh} + DE_{vs} + DE_{vg} + NU_{vi}), \quad (A4)$$

$$S_{qc} = CD_{vc} + ML_{ic} - (CN_{cr} + CL_{cr} + P_{ci} + CL_{ci} + CL_{cs} + CL_{cg} + CL_{ch}), \quad (A5)$$

$$S_{q_r} = \text{CN}_{cr} + \text{CL}_{cr} + \text{ML}_{ir} + \text{ML}_{sr} + \text{ML}_{gr} + \text{ML}_{hr} - (\text{CL}_{rg} + \text{CL}_{rh} + \text{EV}_{rv}), \quad (\text{A6})$$

$$S_{q_i} = \text{NU}_{vi} + P_{ci} + \text{CL}_{ci} - (\text{CN}_{ig} + \text{SU}_{iv} + \text{CL}_{is} + \text{CL}_{ig} + \text{CL}_{ih} + \text{CN}_{is}), \quad (\text{A7})$$

$$S_{q_s} = \text{CN}_{is} + \text{CL}_{is} + \text{CL}_{cs} - (\text{ML}_{sr} + \text{CL}_{sg} + \text{CL}_{sh} + \text{CN}_{sg}), \quad (\text{A8})$$

$$S_{q_g} = \text{CN}_{ig} + \text{CN}_{sg} + \text{NU}_{rg} + \text{CL}_{ig} + \text{CL}_{sg} + \text{CL}_{rg} + \text{CL}_{cg} - (\text{CN}_{gh} + \text{CL}_{gh} + \text{SU}_{gv} + \text{ML}_{gr}), \quad \text{and} \quad (\text{A9})$$

$$S_{q_h} = \text{CN}_{gh} + \text{CL}_{ih} + \text{CL}_{sh} + \text{CL}_{gh} + \text{CL}_{rh} + \text{CL}_{ch} - (\text{SU}_{hv} + \text{ML}_{hr}). \quad (\text{A10})$$

The source and sink terms of the number of hydrometeor per unit mass of air in (8) are

$$S_{N_r} = \text{NCN}_{cr} + \text{NML}_{ir} + \text{NML}_{sr} + \text{NML}_{gr} + \text{NML}_{hr} - (\text{NEV}_{rv} + \text{NCL}_{rh} + \text{NCL}_{rg}), \quad (\text{A11})$$

$$S_{N_i} = \text{NNU}_{vi} + \text{NP}_{ci} + \text{NCL}_{ci} - (\text{NCN}_{is} + \text{NCN}_{ig} + \text{NCL}_{is} + \text{NCL}_{ig} + \text{NCL}_{ih} + \text{NSU}_{iv}), \quad (\text{A12})$$

$$S_{N_s} = \text{NCN}_{is} + \text{NCL}_{rs} - (\text{NCL}_{sg} + \text{NCL}_{sh} + \text{NCN}_{sg} + \text{NSU}_{sv} + \text{NML}_{sr}), \quad (\text{A13})$$

$$S_{N_g} = \text{NCN}_{ig} + \text{NCN}_{sg} + \text{NNU}_{rg} - (\text{NCN}_{gh} + \text{NCL}_{gh} + \text{NSU}_{gv} + \text{NML}_{gr}), \quad (\text{A14})$$

and

$$S_{N_h} = \text{NCN}_{gh} - (\text{NSU}_{hv} + \text{NML}_{hr}), \quad (\text{A15})$$

where the first and second subscripts in the right-hand sides of the above equations represent the depleted and increased hydrometeors, respectively; NNU, NCN, NML, NCL, NSU, NDE, and NEV represent the number of hydrometeor per unit mass of air transferred during the microphysical processes of NU, CN, ML, CL, SU, DE, and EV, respectively.

APPENDIX B

Electrical Terms

The source and sink terms of the charge mixing ratio of each hydrometeor in (9) are

$$S_{q_{ce}} = e \left[\left(\frac{\partial n_+}{\partial t} \right)_c^e - \left(\frac{\partial n_-}{\partial t} \right)_c^e \right] - \left(\frac{\partial q_{re}}{\partial t} \right)_p^{r-c} - \left(\frac{\partial q_{he}}{\partial t} \right)_{np}^{h-c} - \left(\frac{\partial q_{ge}}{\partial t} \right)_{np}^{g-c} - \left(\frac{\partial q_{se}}{\partial t} \right)_p^{s-c} - \left(\frac{\partial q_{he}}{\partial t} \right)_p^{h-c}, \quad (\text{B1})$$

$$S_{q_{re}} = e \left[\left(\frac{\partial n_+}{\partial t} \right)_e^r - \left(\frac{\partial n_-}{\partial t} \right)_e^r \right] + \left(\frac{\partial q_{re}}{\partial t} \right)_p^{r-c}, \quad (\text{B2})$$

$$S_{q_{ie}} = e \left[\left(\frac{\partial n_+}{\partial t} \right)_e^i - \left(\frac{\partial n_-}{\partial t} \right)_e^i \right] - \left(\frac{\partial q_{he}}{\partial t} \right)_p^{h-i} - \left(\frac{\partial q_{ge}}{\partial t} \right)_{np}^{g-i} + \left(\frac{\partial q_{ie}}{\partial t} \right)_s^{s-i}, \quad (\text{B3})$$

$$S_{q_{se}} = e \left[\left(\frac{\partial n_+}{\partial t} \right)_e^s - \left(\frac{\partial n_-}{\partial t} \right)_e^s \right] + \left(\frac{\partial q_{se}}{\partial t} \right)_p^{s-c} + \left(\frac{\partial q_{se}}{\partial t} \right)_p^{s-i} - \left(\frac{\partial q_{se}}{\partial t} \right)_{np}^{g-s} - \left(\frac{\partial q_{se}}{\partial t} \right)_{np}^{h-s}, \quad (\text{B4})$$

$$S_{q_{ge}} = e \left[\left(\frac{\partial n_+}{\partial t} \right)_e^g - \left(\frac{\partial n_-}{\partial t} \right)_e^g \right] + \left(\frac{\partial q_{ge}}{\partial t} \right)_p^{g-i} + \left(\frac{\partial q_{ge}}{\partial t} \right)_{np}^{g-i} + \left(\frac{\partial q_{ge}}{\partial t} \right)_p^{g-c} + \left(\frac{\partial q_{ge}}{\partial t} \right)_{np}^{g-c}, \quad \text{and} \quad (\text{B5})$$

$$S_{q_{he}} = e \left[\left(\frac{\partial n_+}{\partial t} \right)_e^h - \left(\frac{\partial n_-}{\partial t} \right)_e^h \right] + \left(\frac{\partial q_{he}}{\partial t} \right)_p^{h-i} + \left(\frac{\partial q_{he}}{\partial t} \right)_{np}^{h-i} + \left(\frac{\partial q_{he}}{\partial t} \right)_p^{h-c} + \left(\frac{\partial q_{he}}{\partial t} \right)_{np}^{h-c}. \quad (\text{B6})$$

Here, $(\partial q_{xe}/\partial t)_p^{x-y}$, $(\partial q_{xe}/\partial t)_{np}^{x-y}$, and $(\partial q_{ie}/\partial t)_s$ represent the inductive, noninductive, and secondary ice electrification processes, respectively, and the superscripts $x-y$ mean that two types of hydrometeors are involved.

The source and sink terms of the number of ions per unit mass of air in (10) are

$$S_{n_{\pm}} = \frac{G}{\rho} - \alpha \rho n_+ n_- - \left(\frac{\partial n_{\pm}}{\partial t} \right)_e^c - \left(\frac{\partial n_{\pm}}{\partial t} \right)_e^i - \left(\frac{\partial n_{\pm}}{\partial t} \right)_e^r - \left(\frac{\partial n_{\pm}}{\partial t} \right)_e^s - \left(\frac{\partial n_{\pm}}{\partial t} \right)_e^g - \left(\frac{\partial n_{\pm}}{\partial t} \right)_e^h. \quad (\text{B7})$$

Here, G is the air density-involved nonthunderstorm ion generation rate ($\text{m}^{-3} \text{s}^{-1}$) and α is the ion-ion recombination coefficient. The superscript x in $(\partial n_{\pm}/\partial t)_e^x$ includes all six hydrometeors (cloud water, cloud ice, rain, graupel, snow, and hail), and the subscript e means the diffusion and selective ion capture electrification processes.

Electrification parameterization

The present model follows the work of Chiu (1978) for parameterizations of ion diffusion and selective ion capture and the work of Hallett and Saunders (1979) for parameterization of charge separation associated with secondary ice crystal production. Parameterization of inductive charging between small and large liquid water drops (i.e., cloud water drops and raindrops) is based on the work of Chiu (1978). The charge transfer between raindrops with radius r_r and cloud drops with radius r_c is represented as

$$\left(\frac{\partial q_{re}}{\partial t}\right)_p^{r-c} = E_{rc}|V_r - V_c|\rho^2 N_c N_r \pi r_r^2 \times [4\pi\epsilon\gamma_1|\mathbf{E}|\cos(\mathbf{E}, \mathbf{V}_{rc})r_c^2\langle\cos\alpha_1\rangle - Aq_{re} + Bq_{ce}]\langle S\rangle, \quad (\text{B8})$$

where E_{rc} is the collision efficiency, V_r and V_c are the mass-weighted average fall speeds of raindrops and cloud drops, respectively, and \mathbf{V}_{rc} is the velocity of raindrops relative to cloud drops. Here, N_c and N_r are the numbers of cloud water and rainwater drops per unit mass of air, respectively; α_1 represents the collision angle; $\langle\cos\alpha_1\rangle$ is the mean value of $\cos\alpha_1$; and $\langle S\rangle$ is the mean separation probability. Positive nondimensional coefficients are represented by A and B , which can be expressed in terms of the ratio between the radii of drops, and γ_1 is a positive nondimensional constant.

Based on the work of Kuettner et al. (1981), (B8) can be also used to parameterize inductive charging between cloud drop and large ice-phase particles (i.e., snow, graupel, and hail) and between ice and hail (or snow, graupel) with different separation probabilities. In the present model, the separation probability for collision between small and large liquid drops is obtained from the work of Chiu (1978), and others are deduced from the work of Helsdon and Farley (1987).

Parameterization of noninductive charging primarily follows the work of Kuettner et al. (1981). The charge transfer between small and large hydrometeors is given by

$$\left(\frac{\partial q_{Le}}{\partial t}\right)_{np}^{L-s} = E_{Ls}|V_L - V_s|\rho^2 N_L N_s \pi r_L^2 \times [A' + (B - 1)q_{Le} + Bq_{se}]\langle S\rangle, \quad (\text{B9})$$

where E_{Ls} denotes the collision efficiency; V_L and V_s are the mass-weighted average fall speeds of large and small hydrometeor particles, respectively; N_L and N_s are the numbers of large and small hydrometeor particles per unit mass of air, respectively; and A' is the charge transferred per collision and is determined following the work of Helsdon and Farley (1987).

APPENDIX C

Lightning Parameterization

The lightning parameterization scheme implemented in the present model is mainly based on the work of Helsdon et al. (1992). The scheme takes into account the initiation, propagation direction, and termination of lightning discharge and the charge rearrangement from the lightning. In the model, the initiation of lightning discharge is activated when the electric field is above a breakdown value of 250 kV m^{-1} . The termination criterion is selected when the electric field is below a threshold value of 150 kV m^{-1} . The propagation direction of lightning discharge is subject to the direction of maximum electric field. The charge rearrangement along the discharge channel is included as follows.

The discharge channel is assumed to be electrically neutral. The linear charge density at a grid point n along the channel can be expressed as

$$Q_n = -\left\{2\pi\epsilon\frac{b^2}{a}\left[\frac{F'_1(a)P_1(x) - F'_3(a)P_3(x)}{f_1(a)P_1(x) - f_3(a)P_3(x)}\right]\right\}(\varphi - \varphi_0), \quad (\text{C1})$$

where

$$f_1(a) = \frac{5R^2a}{3} - \frac{3a^2}{5}, \quad f_3(a) = \frac{2a^3}{3},$$

$$F'_1(a) = f'_1(a) - \frac{f_1(a)}{Q_1(y)}Q'_1(y), \quad \text{and}$$

$$F'_3(a) = f'_3(a) - \frac{f_3(a)}{Q_3(y)}Q'_3(y).$$

Here, $P_1(x)$ and $P_3(x)$ are the Legendre polynomials of the first kind, and $Q_1(y)$ and $Q_3(y)$ are the Legendre polynomials of the second kind; φ denotes the environmental electric potential at the grid point in the lightning channel; and φ_0 is the electric potential at the initiation point of lightning discharge. The primes mean differentiation, R is the radius of the charge-containing sphere, and a and b are the half length and radius of the channel, respectively. The arguments of the Legendre polynomials are $x = z/a$ and $y = a/c$, where $c = (a^2 - b^2)^{1/2}$. Following the procedure described in Helsdon et al. (1992), the linear charge density at a grid point is converted into a volumetric charge density, which is then converted into an equivalent ion number density.

REFERENCES

- Baker, B., M. B. Baker, E. R. Jayaratne, L. Latham, and C. P. R. Saunders, 1987: The influence of diffusional growth rates on the charge transfer accompanying rebounding collisions between ice crystals and hailstones. *Quart. J. Roy. Meteor. Soc.*, **113**, 1193–1215.
- Bateman, M. G., T. C. Marshall, and M. Stolzenburg, 1999: Precip-

- itation charge and size measurements inside a New Mexico mountain thunderstorm. *J. Geophys. Res.*, **104**, 9643–9653.
- Chiu, C.-S., 1978: Numerical study of cloud electrification in an axisymmetric time-dependent cloud model. *J. Geophys. Res.*, **83**, 5025–5049.
- Dye, J. E., and Coauthors, 1986: Early electrification and precipitation development in a small, isolated Montana cumulonimbus. *J. Geophys. Res.*, **91**, 1231–1247.
- Gardiner, B., D. Lamb, R. L. Pitter, J. Hallett, and C. P. R. Saunders, 1985: Measurements of initial potential gradient and particle charges in a Montana summer thunderstorm. *J. Geophys. Res.*, **90**, 6079–6086.
- Hallett, J., and C. P. R. Saunders, 1979: Charge separation associated with secondary ice crystal production. *J. Atmos. Sci.*, **36**, 2230–2235.
- Helsdon, J. H., Jr., and R. D. Farley, 1987: A numerical modeling study of a Montana thunderstorm: 2. Model results versus observations involving electrical aspects. *J. Geophys. Res.*, **92**, 5661–5675.
- , G. Wu, and R. D. Farley, 1992: An intracloud lightning parameterization scheme for a storm electrification model. *J. Geophys. Res.*, **97**, 5865–5884.
- Houze, R. A., Jr., 1993: *Cloud Dynamics*. Academic Press, 573 pp.
- Jayaratne, E. R., C. P. R. Saunders, and J. Hallett, 1983: Laboratory studies of the charging of soft-hail during ice crystal interactions. *Quart. J. Roy. Meteor. Soc.*, **109**, 609–630.
- Jones, J. J., W. P. Winn, and J. E. Dye, 1982: Early electrification in a cumulus. Preprints, *Conf. on Cloud Physics*, Chicago, IL, Amer. Meteor. Soc., 562–565.
- Klemp, J. B., and R. B. Wilhelmson, 1978: The simulation of three-dimensional convective storm dynamics. *J. Atmos. Sci.*, **35**, 1070–1096.
- Kuettner, J. P., Z. Levin, and J. D. Sartor, 1981: Thunderstorm electrification—inductive or non-inductive? *J. Atmos. Sci.*, **38**, 2470–2484.
- MacGorman, D. R., and W. D. Rust, 1998: *The Electrical Nature of Storms*. Oxford University Press, 422 pp.
- Norville, K., M. Baker, and L. Latham, 1991: A numerical study of thunderstorm electrification: Model development and case study. *J. Geophys. Res.*, **96**, 7463–7481.
- Orville, H. D., and F. J. Kopp, 1977: Numerical simulation of the life history of a hailstorm. *J. Atmos. Sci.*, **34**, 1596–1618.
- Schuur, T. J., and S. A. Rutledge, 2000: Electrification of stratiform regions in mesoscale convective systems. Part II: Two-dimensional numerical model simulations of a symmetric MCS. *J. Atmos. Sci.*, **57**, 1983–2006.
- Takahashi, T., 1984: Thunderstorm electrification—a numerical study. *J. Atmos. Sci.*, **41**, 2541–2558.
- Tripoli, G. J., and W. R. Cotton, 1982: The Colorado State University three-dimensional cloud/mesoscale model—1982. Part I: General theoretical framework and sensitivity experiments. *J. Rech. Atmos.*, **16**, 185–219.
- Ziegler, C. L., and D. R. MacGorman, 1994: Observed lightning morphology relative to modeled space charge and electric field distributions in a tornadic storm. *J. Atmos. Sci.*, **51**, 833–851.